

Embedded-atom potential for an accurate thermodynamic description of the iron–chromium system



S.M. Eich*, D. Beinke, G. Schmitz

Institute of Materials Science, University of Stuttgart, Heisenbergstraße 3, D-70569 Stuttgart, Germany

ARTICLE INFO

Article history:

Received 24 February 2015

Received in revised form 26 March 2015

Accepted 27 March 2015

Keywords:

Embedded-atom method (EAM)

Two-band model (TBM)

Iron–chromium (Fe–Cr)

Phase diagram

Isobaric semi-grandcanonical ensemble

Miscibility gap

Effective pair format

ABSTRACT

A new potential for the iron–chromium (Fe–Cr) alloy system was optimized for the embedded-atom method (EAM) within the two-band model (TBM) extension. In contrast to previous works, free model parameters are predominantly adapted to available experimental high-temperature data of the mixing enthalpy. As a major improvement, the metastable α/α' miscibility gap is accurately described in agreement with experimental data and a recent CALPHAD parametrization. The potential was also fitted to obtain an enriched solubility for chromium atoms in an iron matrix at 0 K, as it is predicted by several *ab initio* calculations. Furthermore, it was benchmarked against phonon excess entropies at 300 K and 1600 K demonstrating good agreement with respective results of inelastic neutron scattering.

© 2015 Elsevier B.V. All rights reserved.

1. Introduction

The iron–chromium (Fe–Cr) alloy system is of great technological interest since it is the basis of stainless steels [1] and a promising candidate for fusion or fission reactors and spallation neutron sources [2]. It is also one of the rare systems for which particular properties of triple junctions were measured [3]. Thus, it is important to predict its properties by means of theoretical calculations. Density functional theory (DFT) is not capable of calculating extended microstructural features such as grain boundaries, triple junctions, or even impact collision cascades which comprise several thousands to millions of atoms. For these cases, molecular dynamics (MD) or Monte Carlo (MC) simulations are very helpful tools [4]. The main input of such simulations is an appropriate (many-body) interatomic interaction which has to be designed to model the alloy realistically. Prior attempts of deriving an interatomic potential for Fe–Cr alloys concentrated on the reproduction of theoretical DFT data of the mixing enthalpy [5,6]. However, as different approximations for the exchange correlation functional produce already a significant variation of results [7–11], it is not clear which DFT data should be used as a correct reference. In this work, we therefore follow a different approach: instead of using target values from DFT calculations, we predominantly adapt the

potential to high-temperature experimental data of the mixing enthalpy [12–14]. It turns out that in this way, an appropriate description of the important metastable α/α' phase equilibrium with the embedded-atom method (EAM) is obtained. In particular, the critical temperature of the miscibility gap is matched with high accuracy according to experimental data [15–17] and the general shape of the miscibility gap at lower temperatures is predicted in good agreement with experimental phase diagrams and theoretical expectations [11,18].

Our report is organized as follows: In Section 2, we give a description of the EAM formalism and the methods applied here for the calculation of phase diagrams. Then, in Section 3, we briefly discuss the Fe–Cr potentials previously derived in literature and show their respective phase diagrams in comparison with experimental data and CALPHAD evaluations. In Section 4, we optimize the parametrization of our new potential and explicitly demonstrate that fitting the mixing enthalpy to DFT data results in an inappropriate phase diagram, while adapting to experimental data yields a description of the metastable miscibility gap with comparably high accuracy. We also present excess vibrational entropies calculated by our new EAM potential which are found to be in good agreement with experimental data.

We want to emphasize that all calculations, experimental data, and CALPHAD evaluations presented in this work are restricted to the metastable α/α' phases since the formation of the σ phase is very slow [19] and usually kinetically suppressed by the cooling

* Corresponding author.

E-mail address: Sebastian.Eich@imw.uni-stuttgart.de (S.M. Eich).

rates applied in experiments. For the actual fitting procedure, only direct interaction between iron and chromium was taken into account, while the potentials for pure elements were taken from literature [5,20].

2. Methodology

2.1. Formalism

For a solid consisting of N atoms, the total EAM [21,22] energy is given by

$$U_{\text{tot}} = \frac{1}{2} \sum_{i=1}^N \sum_{j=1, j \neq i}^N V_{t_i t_j}(r_{ij}) + \sum_{i=1}^N F_{t_i}(\bar{\rho}_i), \quad (1)$$

where $V_{t_i t_j}(r_{ij})$ is the pair interaction function between atoms i and j of type t_i and t_j at distance $r_{ij} = |\vec{r}_j - \vec{r}_i|$ and $F_{t_i}(\bar{\rho}_i)$ is the embedding function of type t_i at atomic site i with a local electron density of $\bar{\rho}_i$. The latter is generated by superposition of the electron densities of all surrounding atoms under consideration of their respective type t_j :

$$\bar{\rho}_i = \sum_{j=1, j \neq i}^N \rho_{t_j}(r_{ij}). \quad (2)$$

It has been shown that this EAM formalism is not capable of reproducing a change of sign in the mixing enthalpy [23–25]. Since exactly this feature is important in the Fe–Cr system, the so-called two-band model (TBM) extension has been proposed [26,27] to receive a more realistic description:

$$U_{\text{tot}} = \frac{1}{2} \sum_{i=1}^N \sum_{j=1, j \neq i}^N V_{t_i t_j}(r_{ij}) + \sum_{i=1}^N F_{t_i}^d(\bar{\rho}_i^d) + \sum_{i=1}^N F_{t_i}^s(\bar{\rho}_i^s). \quad (3)$$

A second embedding function has been added here. This may be interpreted as the particular impact of a second electron band. However, since the detailed physical justification is difficult, it is better considered as a formal concept to take into account the second order influence of the central atom on the local electron intensity. Nevertheless, we will designate in the following the two terms as contributions of the d- and s-electrons. It should be noted that the single electron contributions of the s-electron density $\bar{\rho}_i^s$ need to be defined in a more general way to allow for the desired change of sign of the mixing enthalpy:

$$\bar{\rho}_i^s = \sum_{j=1, j \neq i}^N \rho_{t_i t_j}^s(r_{ij}), \quad (4)$$

i.e., the single s-electron density depends both on the type of the respective neighbor atom t_j and the type of the central atom t_i . Conventionally, it is assumed that atomic pairs of the same type do not contribute to the total s-electron density:

$$\rho_{t_i t_j}^s(r_{ij}) = 0 \quad \text{for} \quad t_i = t_j, \quad (5)$$

while unlike pairs also fulfill the symmetry relation

$$\rho_{t_i t_j}^s(r_{ij}) = \rho_{t_j t_i}^s(r_{ji}). \quad (6)$$

This convenient choice has the important advantage that previously optimized EAM potentials of pure elements can be further used without any modification when a general potential for an alloy should be constructed. So within the TBM, the only additional functions to model the binary AB alloy are the pair interaction function V_{AB} for unlike atomic species, the two s-embedding functions F_A^s and F_B^s , respectively, and the s-electron density ρ_{AB}^s . All other contributions are already known from the pure components.

2.1.1. Effective pair format

In the standard EAM formalism, an effective pair format was introduced [28] which allows a straight forward comparison of different potentials. The total energy, Eq. (1), is invariant under the transformation

$$\begin{aligned} \tilde{F}(\bar{\rho}) &= F(\bar{\rho}) - k\bar{\rho} \\ \tilde{V}(r) &= V(r) + 2k\rho(r), \quad k \in \mathbb{R}. \end{aligned} \quad (7)$$

Thus, by setting

$$k := \left. \frac{dF(\bar{\rho})}{d\bar{\rho}} \right|_{\bar{\rho}=\bar{\rho}_0} = F'(\bar{\rho}_0), \quad (8)$$

the derivative of the embedding function vanishes for the equilibrium electron density $\bar{\rho}_0$. Furthermore, the equilibrium electron density is usually fixed to unity which is easily achieved by proper inverse scaling of the electron density and the argument of the embedding function.

Owing to the specific formulation of the TBM, we can define a similar effective pair format for the interaction between unlike species as well. For comparison of different potentials, we consider a statically ordered $A_{0.5}B_{0.5}$ alloy (although it may not be energetically favored as in the case of Fe–Cr). Required by Eq. (6), the s-electron density is the same at every atomic equilibrium site of the ordered alloy so that all derivatives of the s-embedding functions vanish after transformation. The entire additional contribution stemming from interaction between unlike species is then simply given by

$$U_{\text{alloy}} = \frac{N}{2} \sum_{i=2}^N V_{AB}(r_i) + \frac{N}{2} (F_A^s(\bar{\rho}^s) + F_B^s(\bar{\rho}^s)), \quad (9)$$

where the prime indicates that only interactions between unlike species are taken into account. It can be easily proven that the following transformation holds for the TBM:

$$\begin{aligned} \tilde{F}_i^s(\bar{\rho}^s) &= F_i^s(\bar{\rho}^s) - k_i \bar{\rho}^s \\ \tilde{V}_{AB}(r) &= V_{AB}(r) + (k_A + k_B) \rho_{AB}^s(r), \quad k_i \in \mathbb{R}. \end{aligned} \quad (10)$$

Again, by defining

$$k_i := \left. \frac{dF_i^s(\bar{\rho}^s)}{d\bar{\rho}^s} \right|_{\bar{\rho}^s=\bar{\rho}_0^s}, \quad (11)$$

the derivatives of the s-embedding functions vanish for the transformed potentials in equilibrium. We also rescale the s-electron density ρ_{AB}^s so that the total s-electron density $\bar{\rho}_0^s$ becomes equal to unity for the given structure.

2.2. Calculation of phase diagrams

In order to calculate binary phase diagrams for a given interatomic potential, MC simulations are carried out in the constant ($\Delta\mu NpT$) semi-grandcanonical ensemble. For a cubic box size with volume V and length L ($dV = 3L^2 dL$) and using scaled particle coordinates within that box ($d\vec{r}_i = L^3 d\vec{s}_i$), the partition function is given by

$$\begin{aligned} Z_{\mu_A, \mu_B, N, p, T}(\{\vec{s}_i\}, c, L) &= \frac{3}{\Lambda_A^{3N}} \exp(\beta\mu_A N) \\ &\times \sum_{\mathcal{P}(\{\vec{s}_i\})} \int_{[0,1]^{3N}} \int_0^\infty \int_0^1 dc dL d^N \vec{s} \\ &\times e^{-\beta(U(\{\vec{s}_i\}) + pL^3 - Nc\mu) + (3N-1) \ln L + \frac{3Nc}{2} \ln \frac{m_B}{m_A}}, \end{aligned} \quad (12)$$

in which the independent variables are the scaled particle positions $\{\vec{s}_i\}$ within the simulation box, the concentration c of component B , and the cubic box length L . The prefactor is extracted for

convenience and contains the thermal wavelength $\Lambda_A = h/\sqrt{2\pi m_A k_B T}$. The summation takes into account all different permutations $\mathcal{P}(\{\tilde{S}_i\})$ of the atomic idle positions $\{\tilde{S}_i\}$ which corresponds to the configurational part. Every state is weighted according to its Boltzmann factor which contains the total EAM/TBM potential energy U and also a term containing the atomic masses m_i which is related to the vibronic part. (Note that in isobaric ensembles an additional factor of $1/L^3$ has to be added to the partition function to account for the density of volume states [29–32] which is usually referred to as *volume scale* in literature.)

From the above partition function, we derive the Metropolis [33] acceptance probability which naturally obeys detailed balance

$$A = \min \left(1, e^{-\beta \left(\Delta U + p \Delta L^3 - N \Delta c \left(\Delta \mu + \frac{3}{2\beta} \ln \frac{m_B}{m_A} \right) + \frac{1}{\beta} \ln \frac{L_f}{L_i} \right)} \right), \quad (13)$$

where L_i and L_f denote the initial and final cubic box sizes, respectively. MC trial moves allow particle displacement ($\{\tilde{S}_i\}$), volume change (L), and concentration change (c). (Note here also that the Markov chain is not symmetric if volume trial moves are performed. The proposal probability for a volume change is equal to $1/L^3$ which cancels out the $3N \ln L$ from the partition function. This is also the reason why the MC simulation has to be performed on scaled coordinates. Otherwise, the transition probability cannot be evaluated since different volumes are mapped to each other. The correction in the acceptance probability resulting from the volume scale is rather small, but in isobaric benchmarking MC calculations, the applied pressure is better reproduced if the volume scale is taken into account. To the best of our knowledge, a detailed derivation for the acceptance probability in the isobaric semi-grandcanonical ensemble is not available in literature, although it is the common ensemble for phase diagram calculations. However, running MC simulations with special cases of Eq. (13) always yields perfect agreement with respective MD results, where applicable.)

Average concentrations of the system for given values of $\Delta \mu = \mu_B - \mu_A$ are then determined by rather long MC runs. (We make sure that for the standard error of the average $\Delta c < 5 \times 10^{-4}$ holds.) Since the resulting $\Delta \mu(c)$ curves reveal a significant hysteresis within the miscibility gap (see also Fig. 7a)), one cannot obtain the equilibrium solubilities from these curves directly. Therefore, we apply the common procedure (see e.g. [34,35]) which involves modeling the Gibbs free energy of the system by a Redlich–Kister (RK) expansion [36]

$$\begin{aligned} G(c, T) = & cG^{(A)}(T) + (1-c)G^{(B)}(T) \\ & + k_B T (c \ln c + (1-c) \ln(1-c)) \\ & + c(1-c) \sum_i L_i(T) (2c-1)^i \end{aligned} \quad (14)$$

with free coefficients L_i . By taking the derivative with respect to concentration

$$\Delta \mu(c, T) = -\frac{\partial G(c, T)}{\partial c}, \quad (15)$$

we get an analytical expression for the $\Delta \mu(c)$ curves which is then fitted to the averaged MC results to determine the L_i expansion coefficients of Eq. (14). (To maintain physical behavior, we additionally constrain the fourth derivative of the Gibbs free energy to be positive.)

As can be seen from Eqs. (14) and (15), the expression for the chemical potential difference does not only contain the free fitting parameters L_i , but also the difference of the Gibbs free energies of the pure components ΔG which determines the absolute height of the $\Delta \mu$ curve. Therefore, the Gibbs free energies of the pure components need to be known exactly.

Finally, by applying the common tangent construction to the Gibbs free energy of Eq. (14), we obtain the equilibrium phase concentrations. It should be mentioned here that the described calculation of phase diagrams does not rely on any physical approximations. The only source of errors are of numerical or statistical nature.

2.3. Calculation of Gibbs free energies

In contrast to the enthalpy, the calculation of the Gibbs free energy is a tedious task, since this thermodynamic potential cannot be expressed as a simple ensemble average. Several methods have been proposed to get an approximation for the Gibbs free energy: quasi-harmonic approximation (QHA) [37], local-harmonic approximation (LHA) [38], and the variational Gaussian (VARGAUSS) [39,40] method. But for the calculation of phase boundaries it is mandatory to determine Gibbs free energies with a high accuracy within 1 meV per atom, or even less. Therefore, exact calculation schemes are needed. Here we carried out simulations with the switching Hamiltonian method, also known as thermodynamic integration [4]: Consider the Hamiltonian of a coupled system $H(\lambda) = \lambda U + (1-\lambda)W$ with a continuous coupling parameter λ and an arbitrary reference system with Hamiltonian W from which the Gibbs free energy is known (e.g. the Einstein crystal of independent oscillators). It can then be shown very easily that the Gibbs free energy of the system of interest with Hamiltonian U is given by

$$G(\lambda = 1) = G(\lambda = 0) + \int_0^1 \langle U - W \rangle_\lambda d\lambda, \quad (16)$$

where $\langle \dots \rangle_\lambda$ denotes the thermodynamic ensemble average of the system with Hamiltonian $H(\lambda)$ and constant λ . Numerical integration is performed with the Gauss–Kronrod–Patterson [41] algorithm with up to 87 abscissae sampling points.

Knowing the exact Gibbs free energy at a reference temperature $G(T_0)$, the Gibbs–Helmholtz equation

$$G(T) = G(T_0) \frac{T}{T_0} - T \int_{T_0}^T \frac{H(T')}{T'^2} dT' \quad (17)$$

is applied to determine the Gibbs free energy at any other temperature. (The temperature dependence of the enthalpy $H(T)$ is easily determined by ensemble averaging.)

Gibbs free energies of the pure components iron and chromium as obtained by the different calculation methods are compared in Fig. 1. The exact methods, switching Hamiltonian and Gibbs–Helmholtz integration, yield consistent results (the Gibbs–Helmholtz curve shown here is obtained with the reference temperature $T_0 = 100$ K, but in fact, any reference from the switching Hamiltonian method must result in the same Gibbs–Helmholtz curve). The approximations deviate by several tens of meV at elevated temperatures which is not acceptable in the determination of phase boundaries. In addition, the parametrization from the SGTE database [42] is shown which summarizes experimental data. The almost perfect match between the experimental data and the exact calculation schemes demonstrate the quality of the EAM potentials of the pure components taken from literature [5,20].

3. Literature review: The Fe–Cr phase diagram

For low temperatures, the Fe–Cr phase diagram can be described as a simple decomposing system if one neglects the stable σ phase, which is often kinetically suppressed [19], and the γ -loop where iron undergoes the allotropic transition from bcc to fcc, which only becomes important at higher temperatures and low chromium content. Fig. 2 shows a compilation of

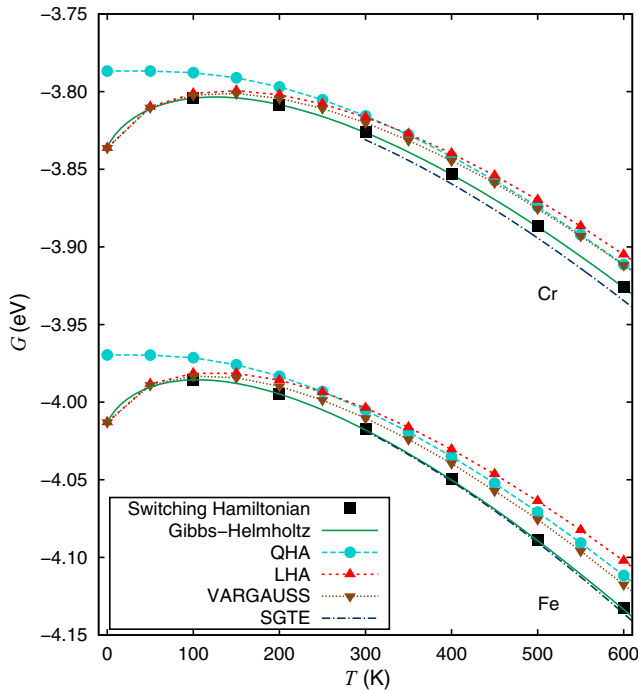


Fig. 1. Temperature dependence of Gibbs free energies of iron [20] and chromium [5] calculated with different methods. While the switching Hamiltonian method and Gibbs-Helmholtz equation yield exact values, the quasi-harmonic approximation (QHA), local-harmonic approximation (LHA), and variational Gaussian method (VARGAUSS) only yield approximations. For QHA, LHA, and VARGAUSS symbols are connected with lines to guide the eyes. Free energy parametrization from the SGTE database is shifted by $H(298.15 \text{ K})$ predicted by the corresponding potential. Note that only the QHA also incorporates zero-point oscillations which become important when approaching 0 K.

measured equilibrium concentrations (symbols) [15–17], different CALPHAD representations [18,43,44] of the metastable miscibility gap, and the phase boundaries predicted by the previously available EAM potentials for the Fe–Cr system [5,6]. Since no experimental data are available below 700 K, it is not clear whether there is indeed an enriched solubility of chromium in an iron matrix, as it is indicated by several DFT calculations [7–11]. Both EAM potentials [5,6] and also the recent CALPHAD parametrization by Bonny [18] take such an increased solubility on the iron-rich side into account, while the other CALPHAD representations do not. (A detailed review of the stable and metastable Fe–Cr phase diagram can be found in Refs. [44,45].)

Besides this controversy, one can clearly notice that the existing EAM potentials do not describe the metastable Fe–Cr system correctly. Calculated with the Olsson potential [5], the miscibility gap closes about 200 K below the experimental critical temperature and an artificial enriched solubility is predicted on the chromium-rich side as well. The latter is simply due to the fact that Olsson et al. used a strictly symmetric approach with respect to composition, i.e. the same s -embedding function for both iron and chromium. By contrast, the critical temperature of the Bonny potential [6] is about 300 K too high and the solubility on the chromium-rich side is way too low at intermediate temperatures. A further shortcoming of the Bonny potential is already due to the underlying potential of pure chromium for which the elastic constant C' yields 77.7 GPa instead of the correct value of 155 GPa. (The pure iron potential was taken from the work of Mendelev et al. [46] and does not show such a discrepancy.)

The above mentioned insufficiencies of existing EAM potentials motivate us to determine a new parametrization in this work which describes the metastable miscibility gap in an appropriate manner.

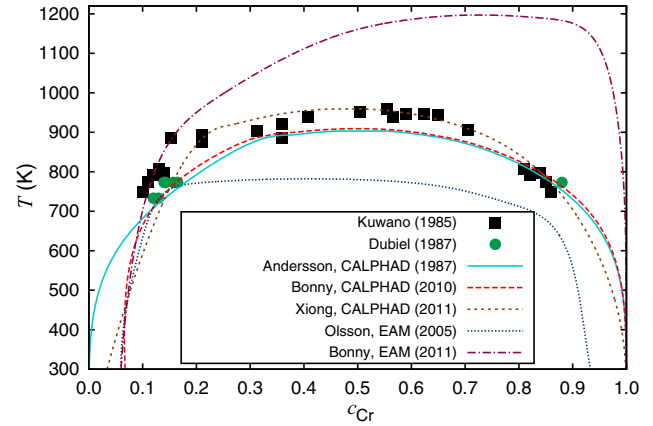


Fig. 2. Comparison of experimental data [15–17], different CALPHAD parameterizations [18,43,44], and existing EAM potentials [5,6] describing the metastable phase boundary of the Fe–Cr system.

4. Derivation of the new potential

4.1. Fitting procedure

For representing the optimized alloy potential, we follow the formal scheme of Olsson et al. [5], but determine a new parameter set by adapting to measured mixing enthalpies [12–14]. As explained in Subsection 2.1, the respective parts of the pure elements are not modified by the chemical interaction. We therefore rely on the EAM potentials for pure chromium derived by Olsson et al. [5] and for pure iron determined by Ackland [20]. Not least, the quality of these potentials are confirmed by the excellent agreement to SGTE data as shown in Fig. 1 provided the Gibbs free energy is calculated by a correct method.

The pair interaction between iron and chromium is described by

$$V_{\text{FeCr}}(r) = \sum_{i=1}^4 a_i (r - r_i)^3 H(r_i - r), \quad (18)$$

where a_i are spline coefficients, r_i are cutoffs, and $H(r)$ is the Heaviside step function. The embedding functions for the s -electron densities are modeled as

$$F_{t_i}^s(\bar{\rho}^s) = A_{t_i,1} \sqrt{\bar{\rho}^s} + A_{t_i,2} (\bar{\rho}^s)^2 + A_{t_i,3} (\bar{\rho}^s)^4, \quad (19)$$

where type t_i is either Fe or Cr, and the $A_{t_i,j}$ are fitting parameters. The s -electron density function is fixed and given by

$$\rho_{\text{FeCr}}^s(r) = (N_s r^3 e^{-\zeta_s r})^2, \quad (20)$$

with $N_s = 5.0 \text{ \AA}^{-3}$ and $\zeta_s = 2.5 \text{ \AA}^{-1}$. In order to provide a smooth cut-off at $r_{\text{cut}} = 5.3 \text{ \AA}$, we apply the following modification [47]:

$$\hat{\rho}_{\text{FeCr}}^s(r) = \rho_{\text{FeCr}}^s(r) - \rho_{\text{FeCr}}^s(r_{\text{cut}}) + \frac{r_{\text{cut}}}{20} \left(1 - \left(\frac{r}{r_{\text{cut}}} \right)^{20} \right) \frac{d\rho_{\text{FeCr}}^s(r)}{dr} \bigg|_{r=r_{\text{cut}}}. \quad (21)$$

For each fitting trial, we used the parameter values provided by Olsson as a starting point, but applied an additional random offset of $\pm 5\%$ to get different initial positions in the parameter space. Multidimensional minimization is performed with the stable simplex algorithm [48], since for a gradient method [49], the structures would have to be equilibrated with very high accuracy to evaluate correct derivatives. The convergence criterion for minimization was defined by

Table 1

Potential parameters obtained by fitting to rescaled DFT mixing enthalpy values according to the second fitting approach. Note that these values are not in the effective pair format.

<i>i</i>	1	2	3	4
$A_{\text{Fe},i}$ (eV)	−0.456106795	−0.626367220	0.560182672	
$A_{\text{Cr},i}$ (eV)	−0.230762957	−0.871017452	0.533468396	
r_i (Å)	2.356834348	2.855258825	3.427273294	5.163521546
a_i (eV/Å ³)	−3.045810917	−0.476426146	−0.598682209	0.012728054

$$\sigma = \sqrt{\frac{1}{n} \sum_i \left(\frac{X_i}{Y_i} - 1 \right)^2} < 0.01, \quad (22)$$

where Y_i is the target value of any desired property and X_i is the corresponding value predicted by the current potential parameters. This can be interpreted as a relative standard deviation of 1% for the accuracy of the target values. This procedure had been repeated until a set of 20 different potentials was generated for a detailed evaluation.

Since the calculation of phase boundaries is too complex, one cannot directly fit the potentials to the phase boundary. Instead, we restrict to very few target values of the mixing enthalpy and check afterwards whether the properties of the derived potential are appropriate. Thus, for the actual fitting procedure, we used only three target values to model the shape of the mixing enthalpy. The first target point is set at $c = 0.0625$ to capture the enriched solubility of chromium in an iron matrix, the second one is set at $c = 0.5$ to capture the maximum of the mixing enthalpy, and the last target value is set at $c = 0.875$, just to have another supporting point for the mixing enthalpy. It turned out that these three points are sufficient to capture the shape of the mixing enthalpy over the whole concentration range (see also Fig. 6).

In a first fitting approach we used the recent DFT values of the mixing enthalpy obtained by Ruban et al. [11] as target values (referenced below as first fitting approach). Since this procedure yields an unacceptable description of the miscibility gap, in a second approach we rescaled the target values to match the measured experimental mixing enthalpy at higher temperatures, but nevertheless to keep the significant solubility of chromium in an iron matrix at 0 K (referenced below as second fitting approach). It will be shown that the latter approach improves the reproduction of the metastable experimental phase diagram significantly. Since we obtained for each approach a total of 20 variants of the potentials and there is of course some scatter in the resulting phase diagrams, we restrict our presentation to a typical variant for the first fitting approach and present the potential with the best agreement with experiment for the second fitting approach.

4.2. New iron–chromium potentials

The resulting potential parameters from the second fitting approach are presented in Table 1 and in Figs. 3–5 we show the corresponding potential curves after transformation into the effective pair format. The pair potential (Fig. 3) generated in this work is very similar to the one from Olsson [5]. In view of Eq. (20), one may expect the s-electron density (see Fig. 4) even to be identical. However, one has to keep in mind that the s-electron density is rescaled so that $\bar{\rho}_0^s = 1$ in equilibrium for the ordered $\text{Fe}_{0.5}\text{Cr}_{0.5}$ alloy. Since the equilibrium lattice parameter slightly differs from Olsson's result, we end up in slightly different s-electron densities. Compared to the embedding functions of the pure elements, the contribution from embedding functions for the s-band are comparably small (see Fig. 5). It is also interesting that the s-embedding function for chromium shows a maximum in equilibrium.

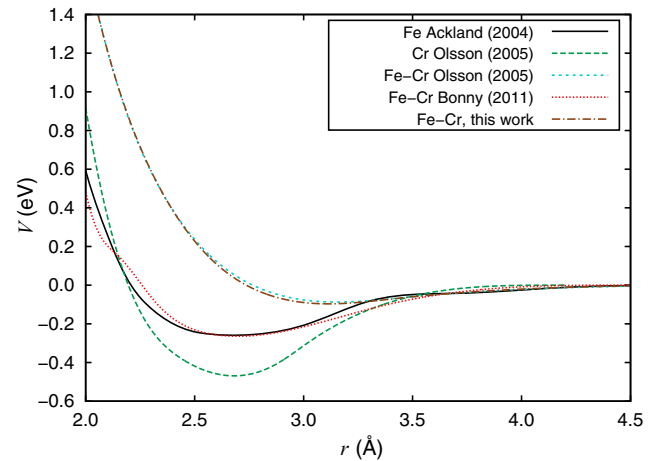


Fig. 3. Comparison of pair interaction functions in the effective pair format.

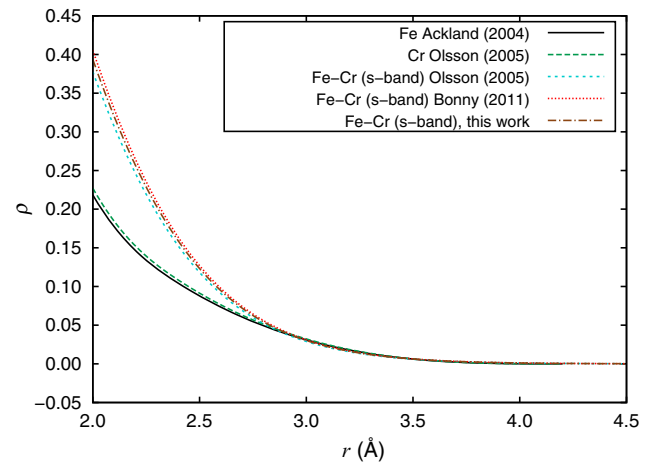


Fig. 4. Comparison of electron density functions in the effective pair format.

4.3. Mixing enthalpies

In Fig. 6, the mixing enthalpies calculated with our potentials are presented together with the respective target values. For the first fitting approach, we used the original DFT values calculated by Ruban et al. [11] which reflect the enriched solubility for chromium atoms in iron. As expected, the model curve derived from our potential (solid black line) matches the target points (squares) perfectly. Since it turned out that fitting to original DFT values does not reveal a reasonable agreement with the experimental phase diagram, we decided to rescale the target values so that they match experimental observations for concentrations with $c_{\text{Cr}} > 0.3$ (triangles) [12–14] but still keeping the significant solubility on the iron side (green circles). Enthalpy curves calculated with this potential according to the second approach match experimental data well

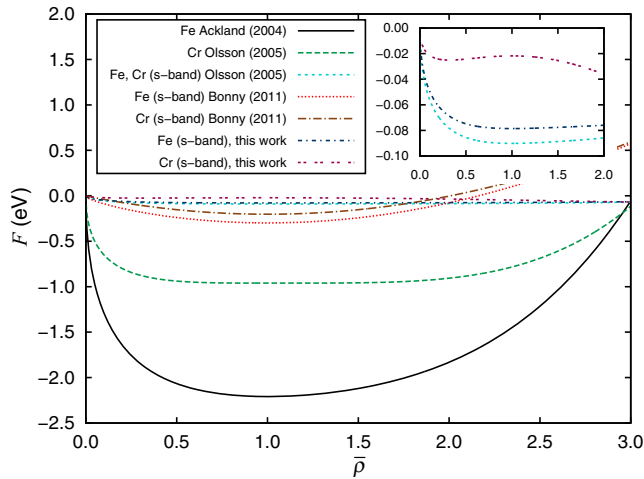


Fig. 5. Comparison of embedding functions in the effective pair format.

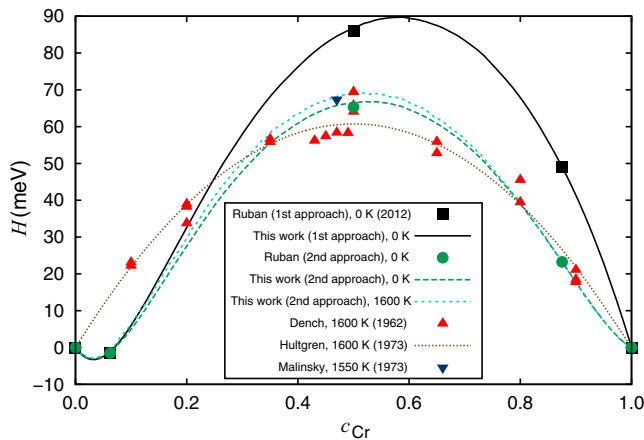


Fig. 6. Comparison of mixing enthalpies: DFT target values according to the first fitting approach (squares) [11], rescaled target values according to the second fitting approach (circles), values predicted by the potentials (lines), and experimental values [12–14].

(dashed lines). Although experimental values for the mixing enthalpy are only available for comparably high temperatures (around 1600 K), this approach works remarkably well, since the temperature dependence of the mixing enthalpy is very weak (compare e.g. the model curves calculated with the second approach for 0 K and 1600 K).

4.4. Phase diagrams

Exemplary $\Delta\mu(c)$ curves as obtained by MC simulations for the optimum potential obtained with the second approach (parameters in Table 1) are shown in Fig. 7a, together with fitted curves for the analytical model expressed by Eq. (15). Three exemplary temperatures are presented: within the miscibility gap (600 K), slightly below the critical temperature of the miscibility gap (950 K), and far above the miscibility gap (1600 K). Knowing the RK expansion coefficients, we can directly plot the Gibbs free energy and apply the common tangent construction to obtain the equilibrium concentrations at the given temperature (Fig. 7b).

When the temperature approaches the critical temperature of the miscibility gap, the $\Delta\mu(c)$ curves become extremely flat so that a comparably high order in the RK expansion is necessary to obtain a good fit. As a direct consequence, the Gibbs free energy is almost

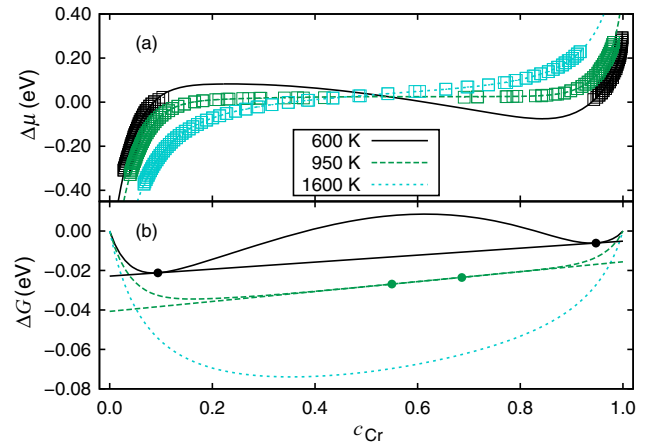


Fig. 7. (a) $\Delta\mu(c_{Cr})$ curves obtained from MC simulations (empty squares) and corresponding fit according to Eq. (15) within the miscibility gap (600 K), slightly below the critical temperature of the miscibility gap (950 K), and far above the miscibility gap (1600 K). (b) Respective Gibbs free energies including common tangent construction. Equilibrium concentrations are marked by circles. Note that only the excess is shown.

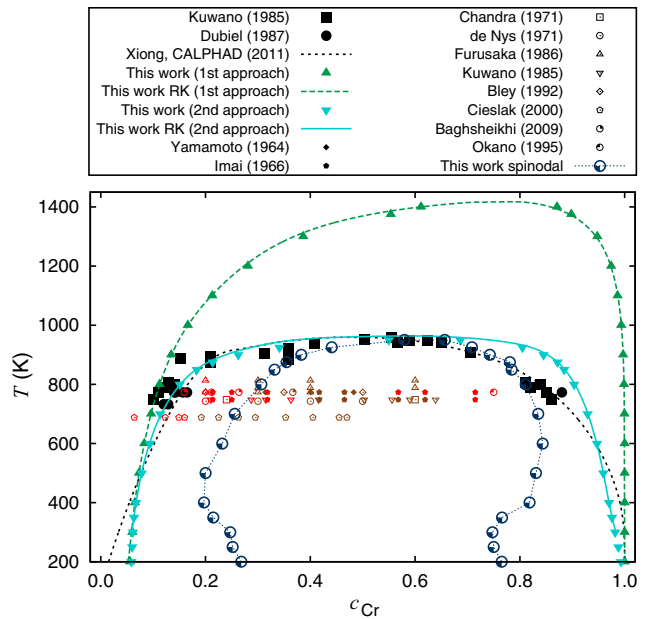


Fig. 8. Experimental data points [15–17] (black symbols) indicating the metastable α/α' miscibility gap together with a recent CALPHAD parametrization [44] (shortly dashed black). Dark green symbols and dashed line reflect the phase boundary obtained with the mixing enthalpy fitted to original DFT data [11] according to the first fitting approach (compare Fig. 6). Light blue symbols and solid line show the most accurate phase boundary obtained with the mixing enthalpy fitted to the rescaled target points according to the second fitting approach (compare Fig. 6). Experimental data points [50–59] indicating the boundary between nucleation and growth regime (red) and spinodal decomposition (brown) are shown in comparison with the spinodal predicted by this work (dark blue symbols). Lines (RK) are calculated with the full Gibbs free energy parametrization as discussed in Appendix A. (For interpretation of the references to colour in this figure legend, the reader is referred to the web version of this article.)

a straight line over a wide range of concentrations so that the common tangent construction cannot be resolved by eyes.

In Fig. 8, phase diagrams resulting from this work are shown in comparison with experimental data on the phase boundaries [15–17] and a CALPHAD evaluation [44] (black). It becomes quite obvious that the potential of our first approach, fitted to the DFT enthalpy data of Ruban et al. [11] (dark green) predicts an

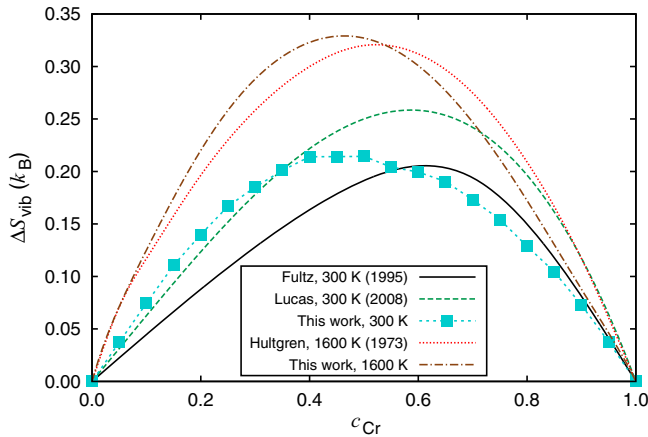


Fig. 9. Excess vibrational entropies at 300 K and 1600 K in comparison with experimental data [14,60,61]. Values calculated at 300 K within the LHA for distinct concentrations are connected with lines.

unacceptable miscibility gap with unacceptable deviation from experimental data, while the second approach, adapted to experimental data of the mixing enthalpy [12–14] – though at high experimental temperature – yields a quite convincing description of the miscibility gap (light blue). In particular, on the iron-rich side, the agreement is remarkably good, while some deviation is still seen for chromium concentrations higher than around 60%.

Since there are no low-temperature equilibrium concentrations available from experiments, we tend to follow *ab initio* DFT calculations [7–11] at 0 K indicating an enriched solubility of chromium in the iron matrix. Thus, our optimum potential reflects a solubility of about 5–6%. We also investigated the spinodal of the potential of the second approach. This spinodal (dark blue) might be compared to experimental data [50–59] which indicate the boundary between the regimes of nucleation and growth (red) and the regime of spinodal decomposition (brown). Our potential reproduces this boundary particularly well on the iron-rich side, while for the chromium-rich side, the width of the spinodal regime appears still to be slightly overestimated. We also tried to fine-tune the target value of the mixing enthalpy on the chromium-rich side ($c = 0.875$) for a better positioning of the boundary for high chromium concentrations at elevated temperatures. Unfortunately, every attempt to increase the solubility of iron in chromium always resulted in a significantly higher solubility also at lower temperatures. The potential presented here reflects the best compromise.

In summary, we can say that according to the aim of the fitting, our potential shows a remarkable improvement over the previously available ones in literature, especially the critical temperature of the miscibility gap (960 K) describes the real system with high accuracy (see also Fig. 2).

4.5. Excess vibrational entropies

The excess vibrational entropy is another physical quantity which can be accessed quite easily. We compare the values predicted by our potential with experimental values at 300 K [60,61] and 1600 K [14] (see Fig. 9). For the higher temperature, we can extract the vibrational entropy directly from the Gibbs free energy and enthalpy, respectively (see Fig. 6 and 7). As for the experimental data, the vibrational excess entropy is almost symmetric, while our potential shows a small shift to the left. But the overall agreement in the quantitative level is excellent.

The calculation of the excess vibrational entropy for 300 K over the whole concentration range cannot be done directly. Since we are deep in the miscibility gap, the $G(c, T)$ curve only takes into account data from MC simulations for the stable phases outside the miscibility gap. Thus, we decided to calculate the Gibbs free energies within the LHA which should give sufficient accuracy at that low temperature. Already the available two experimental data sets [60,61] show some scatter among each other. Again, we see that the position of the maximum of the predicted entropy is slightly shifted to the left, but the magnitude of the maximum is in very good agreement with the experimental range.

5. Summary

In this work we have fitted new iron–chromium (Fe–Cr) alloy potentials in the embedded-atom method (EAM)/two-band model (TBM) formalism. We have demonstrated that fitting the mixing enthalpy to recent density functional theory (DFT) data is not the best choice since the critical temperature of the miscibility gap clearly depends on the height of the maximum of the mixing enthalpy. Thus, we decided to fit the mixing enthalpy to experimental data of high-temperature measurements as the temperature nearly does not affect the mixing enthalpy (the additional energy per atom scales roughly with $3k_B T$). The critical temperature of the miscibility gap of the optimized potential is in remarkable agreement with the experimentally observed one and the potential also shows the desired enriched solubility of chromium atoms in the iron matrix. Furthermore, we investigated the excess vibrational entropy as predicted by our potential and we could demonstrate very good agreement with experimental studies at 300 K and 1600 K.

Appendix A. Full temperature parametrization of Gibbs free energies

According to Eq. (14), the fitting parameters $L_i(T)$ are temperature dependent. To model the full temperature parametrization for the Gibbs free energy, we apply the following CALPHAD-like parametrization to $L_i(T)$:

$$L_i(T) = \alpha_i + \beta_i T^{-1} + \gamma_i T + \delta_i T^2 + \epsilon_i T^3 + \phi_i T \ln T, \quad (23)$$

Table 2

Full Gibbs free energy parametrization for the optimum potential according to Eqs. (14) and (23). The parameters are valid within $300 \text{ K} < T < 1600 \text{ K}$.

	α (eV)	β (eV K)	γ (eV K ⁻¹)	δ (eV K ⁻²)	ϵ (eV K ⁻³)	ϕ (eV K ⁻¹)
L_0	-1.05413×10^1	1.32745×10^3	1.15477×10^{-1}	1.19929×10^{-5}	-1.57894×10^{-9}	-1.68742×10^{-2}
L_1	7.76973×10^{-1}	-1.78952×10^2	2.68477×10^{-3}	1.75578×10^{-6}	-3.62345×10^{-10}	-6.70070×10^{-4}
L_2	4.12268×10^1	-4.43947×10^3	-4.77631×10^{-1}	-5.13247×10^{-5}	6.74307×10^{-9}	7.02656×10^{-2}
L_3	2.66352×10^1	-2.55575×10^3	-3.27988×10^{-1}	-3.70438×10^{-5}	4.98604×10^{-9}	4.86431×10^{-2}
L_4	-1.21626×10^1	1.47663×10^3	1.22866×10^{-1}	1.10673×10^{-5}	-1.27989×10^{-9}	-1.76676×10^{-2}
L_5	-1.21388×10^2	1.20830×10^4	1.45160	1.58266×10^{-4}	-2.07968×10^{-8}	-2.14216×10^{-1}
L_6	-7.75633×10^1	6.73160×10^3	9.91429×10^{-1}	1.13419×10^{-4}	-1.51838×10^{-8}	-1.47493×10^{-1}
L_7	1.79997×10^2	-1.72221×10^4	-2.21586	-2.49251×10^{-4}	3.34172×10^{-8}	3.28472×10^{-1}
L_8	6.42002×10^1	-5.53625×10^3	-8.20487×10^{-1}	-9.26850×10^{-5}	1.22584×10^{-8}	1.21898×10^{-1}
L_9	-9.56629×10^1	8.70365×10^3	1.21802	1.40945×10^{-4}	-1.91779×10^{-8}	-1.81361×10^{-1}

where the parameters α_i , β_i , γ_i , δ_i , ϵ_i , and ϕ_i are obtained by a further fitting process. The full list of parameters for the optimum potential is presented in Table 2.

References

- [1] D. Peckner, I.M. Bernstein, *Handbook of Stainless Steels*, McGraw-Hill, New York, NY, 1977.
- [2] L. Mansur, A. Rowcliffe, R. Nanstad, S. Zinkle, W. Corwin, R. Stoller, J. Nucl. Mater. 329–333 (Part A) (2004) 166–172, <http://dx.doi.org/10.1016/j.jnucmat.2004.04.016>. Proceedings of the 11th International Conference on Fusion Reactor Materials (ICFRM-11).
- [3] P. Stender, Z. Balogh, G. Schmitz, Phys. Rev. B 83 (2011) 121407, <http://dx.doi.org/10.1103/PhysRevB.83.121407>.
- [4] D. Frenkel, B. Smit, *Understanding Molecular Simulation: From Algorithms to Applications*, vol. 1, Academic press, 2001.
- [5] P. Olsson, J. Wallenius, C. Domain, K. Nordlund, L. Malerba, Phys. Rev. B 72 (2005) 214119, <http://dx.doi.org/10.1103/PhysRevB.72.214119>.
- [6] G. Bonny, R. Pasianot, D. Terentyev, L. Malerba, Philos. Mag. 91 (2011) 1724–1746, <http://dx.doi.org/10.1080/14786435.2010.545780>.
- [7] P. Olsson, I. Abrikosov, L. Vitos, J. Wallenius, J. Nucl. Mater. 321 (2003) 84–90, [http://dx.doi.org/10.1016/S0022-3115\(03\)00207-1](http://dx.doi.org/10.1016/S0022-3115(03)00207-1).
- [8] P. Olsson, I.A. Abrikosov, J. Wallenius, Phys. Rev. B 73 (2006) 104416, <http://dx.doi.org/10.1103/PhysRevB.73.104416>.
- [9] T.P.C. Klaver, R. Drautz, M.W. Finnis, Phys. Rev. B 74 (2006) 094435, <http://dx.doi.org/10.1103/PhysRevB.74.094435>.
- [10] P. Erhart, B. Sadigh, A. Caro, Appl. Phys. Lett. 92 (2008), <http://dx.doi.org/10.1063/1.2907337>.
- [11] A.V. Ruban, V.I. Razumovskiy, Phys. Rev. B 86 (2012) 174111, <http://dx.doi.org/10.1103/PhysRevB.86.174111>.
- [12] I. Malinsky, F. Claisse, J. Chem. Thermodyn. 5 (1973) 615–622, [http://dx.doi.org/10.1016/S0021-9614\(73\)80002-3](http://dx.doi.org/10.1016/S0021-9614(73)80002-3).
- [13] W.A. Dench, Trans. Faraday Soc. 59 (1963) 1279–1292, <http://dx.doi.org/10.1039/TF9635901279>.
- [14] R. Hultgren, P.D. Desai, D.T. Hawkins, M. Gleiser, K.K. Kelley, Selected values of the thermodynamic properties of binary alloys, Technical Report, DTIC Document, 1973.
- [15] S. Dubiel, G. Inden, Z. Metallkd. 78 (1987) 544–549.
- [16] S. Dubiel, G. Inden, Hyperfine Interact. 51 (1989) 1009–1010, <http://dx.doi.org/10.1007/BF02407818>.
- [17] H. Kuwano, Trans. Jpn. Inst. Met. 26 (1985) 473–481.
- [18] G. Bonny, D. Terentyev, L. Malerba, J. Phase Equilib. Diffus. 31 (2010) 439–444, <http://dx.doi.org/10.1007/s11669-010-9782-9>.
- [19] F. Wever, W. Jellinghaus, Mitt. Kais.-Wilh.-Inst. Eisenforsch. 13 (1931) 143–147.
- [20] G.J. Ackland, M.I. Mendelev, D.J. Srolovitz, S. Han, A.V. Barashev, J. Phys.: Condens. Matter 16 (2004) S2629, <http://dx.doi.org/10.1088/0953-8984/16/27/003>.
- [21] M.S. Daw, M.I. Baskes, Phys. Rev. Lett. 50 (1983) 1285–1288, <http://dx.doi.org/10.1103/PhysRevLett.50.1285>.
- [22] M.S. Daw, M.I. Baskes, Phys. Rev. B 29 (1984) 6443–6453, <http://dx.doi.org/10.1103/PhysRevB.29.6443>.
- [23] G.J. Ackland, V. Vitek, Phys. Rev. B 41 (1990) 10324–10333, <http://dx.doi.org/10.1103/PhysRevB.41.10324>.
- [24] E.M. Lopasso, M. Caro, A. Caro, P.E.A. Turchi, Phys. Rev. B 68 (2003) 214205, <http://dx.doi.org/10.1103/PhysRevB.68.214205>.
- [25] J. Wallenius, P. Olsson, C. Lagerstedt, N. Sandberg, R. Chakarova, V. Pontikis, Phys. Rev. B 69 (2004) 094103, <http://dx.doi.org/10.1103/PhysRevB.69.094103>.
- [26] S.M. Foiles, M.I. Baskes, M.S. Daw, Phys. Rev. B 33 (1986) 7983–7991, <http://dx.doi.org/10.1103/PhysRevB.33.7983>.
- [27] G.J. Ackland, S.K. Reed, Phys. Rev. B 67 (2003) 174108, <http://dx.doi.org/10.1103/PhysRevB.67.174108>.
- [28] R.A. Johnson, Phys. Rev. B 39 (1989) 12554–12559, <http://dx.doi.org/10.1103/PhysRevB.39.12554>.
- [29] P. Attard, J. Chem. Phys. 103 (1995) 9884–9885, <http://dx.doi.org/10.1063/1.469956>.
- [30] K.-K. Han, H.S. Son, J. Chem. Phys. 115 (2001) 7793–7794, <http://dx.doi.org/10.1063/1.1407295>.
- [31] A.F. Jalbout, J. Mol. Struct. 594 (2002) 157–159, [http://dx.doi.org/10.1016/S0166-1280\(02\)00263-4](http://dx.doi.org/10.1016/S0166-1280(02)00263-4).
- [32] D.S. Corti, G. Soto-Campos, J. Chem. Phys. 108 (1998) 7959–7966, <http://dx.doi.org/10.1063/1.476236>.
- [33] N. Metropolis, A.W. Rosenbluth, M.N. Rosenbluth, A.H. Teller, E. Teller, J. Chem. Phys. 21 (1953) 1087–1092, <http://dx.doi.org/10.1063/1.1699114>.
- [34] P.L. Williams, Y. Mishin, J.C. Hamilton, Modell. Simul. Mater. Sci. Eng. 14 (2006) 817, <http://dx.doi.org/10.1088/0965-0393/14/5/002>.
- [35] G. Bonny, R. Pasianot, E. Zhurkin, M. Hou, Comput. Mater. Sci. 50 (2011) 2216–2220, <http://dx.doi.org/10.1016/j.commatsci.2011.02.032>.
- [36] O. Redlich, A.T. Kister, Ind. Eng. Chem. 40 (1948) 345–348, <http://dx.doi.org/10.1021/ie50458a036>.
- [37] A.A. Maradudin, E.W. Montroll, G.H. Weiss, I. Ipatova, *Theory of Lattice Dynamics in the Harmonic Approximation*, vol. 12, Academic Press, New York, 1963.
- [38] S.M. Foiles, Phys. Rev. B 49 (1994) 14930–14938, <http://dx.doi.org/10.1103/PhysRevB.49.14930>.
- [39] R. LeSar, R. Najafabadi, D.J. Srolovitz, J. Chem. Phys. 94 (1991) 5090–5097, <http://dx.doi.org/10.1063/1.460547>.
- [40] R. LeSar, R. Najafabadi, D.J. Srolovitz, Phys. Rev. Lett. 63 (1989) 624–627, <http://dx.doi.org/10.1103/PhysRevLett.63.624>.
- [41] T.N.L. Patterson, Math. Comput. 22 (1968) 847–856, <http://dx.doi.org/10.1090/S0025-5718-68-99866-9>.
- [42] A. Dinsdale, Calphad 15 (1991) 317–425, [http://dx.doi.org/10.1016/0364-5916\(91\)90030-N](http://dx.doi.org/10.1016/0364-5916(91)90030-N).
- [43] J.-O. Andersson, B. Sundman, Calphad 11 (1987) 83–92, [http://dx.doi.org/10.1016/0364-5916\(87\)90021-6](http://dx.doi.org/10.1016/0364-5916(87)90021-6).
- [44] W. Xiong, P. Hedström, M. Selleby, J. Odqvist, M. Thuvander, Q. Chen, Calphad 35 (2011) 355–366, <http://dx.doi.org/10.1016/j.calphad.2011.05.002>.
- [45] W. Xiong, M. Selleby, Q. Chen, J. Odqvist, Y. Du, Crit. Rev. Solid State Mater. Sci. 35 (2010) 125–152, <http://dx.doi.org/10.1080/10408431003788472>.
- [46] M.I. Mendelev, S. Han, D.J. Srolovitz, G.J. Ackland, D.Y. Sun, M. Asta, Philos. Mag. 83 (2003) 3977–3994, <http://dx.doi.org/10.1080/14786430310001613264>.
- [47] A.F. Voter, Los Alamos Unclassified Technical Report # LA-UR 93-3901 (1993), 1993. Unpublished.
- [48] J.A. Nelder, R. Mead, Computer J. 7 (1965) 308–313, <http://dx.doi.org/10.1093/comjnl/7.4.308>.
- [49] R. Fletcher, *Practical Methods of Optimization*, John Wiley & Sons, 2013.
- [50] H. Yamamoto, Jpn. J. Appl. Phys. 3 (1964) 745, <http://dx.doi.org/10.1143/JJAP.3.745>.
- [51] Y. Imai, M. Izumiya, T. Masumoto, Sci. Rep. Res. Inst., Tohoku Univ., Ser. A 18 (1966) 56–69, <http://ci.nii.ac.jp/naid/110004638116/en/>.
- [52] D. Chandra, L. Schwartz, Metall. Trans. 2 (1971) 511–519, <http://dx.doi.org/10.1007/BF02663342>.
- [53] T. de Nys, P. Gielen, Metall. Trans. 2 (1971) 1423–1428, <http://link.springer.com/article/10.1007/BF02913370>.
- [54] M. Furusaka, Y. Ishikawa, S. Yamaguchi, Y. Fujino, J. Phys. Soc. Jpn. 55 (1986) 2253–2269, <http://dx.doi.org/10.1143/JPSJ.55.2253>.
- [55] H. Kuwano, Trans. Jpn. Inst. Met. 26 (1985) 482–491.
- [56] F. Bley, Acta Metall. Mater. 40 (1992) 1505–1517, [http://dx.doi.org/10.1016/0956-7151\(92\)90094-U](http://dx.doi.org/10.1016/0956-7151(92)90094-U).
- [57] J. Cieslak, S.M. Dubiel, B. Sepiol, J. Phys.: Condens. Matter 12 (2000) 6709, <http://dx.doi.org/10.1088/0953-8984/12/30/303>.
- [58] S. Baghsheikhi, Spinodal decomposition in the binary Fe–Cr system, Master's thesis, Royal Institute of Technology, Stockholm, Sweden, 2009.
- [59] R. Okano, K. Hono, K. Takamashi, H. Fujimori, T. Sakurai, J. Appl. Phys. 77 (1995) 5843–5849, <http://dx.doi.org/10.1063/1.359165>.
- [60] B. Fultz, L. Anthony, J.L. Robertson, R.M. Nicklow, S. Spooner, M. Mostoller, Phys. Rev. B 52 (1995) 3280–3285, <http://dx.doi.org/10.1103/PhysRevB.52.3280>.
- [61] M.S. Lucas, M. Kresch, R. Stevens, B. Fultz, Phys. Rev. B 77 (2008) 184303, <http://dx.doi.org/10.1103/PhysRevB.77.184303>.